Check for updates

ADVANCING EARTH AND SPACE SCIENCES

JGR Space Physics

RESEARCH ARTICLE
10.1029/2025JA034303

Correlation Patterns of Muon Flux With Vertical Atmospheric Profiles: Insights From Monte Carlo Simulations

A. Al-Qaaod[1], V. Pierrard[2,3], A. Winant[2,3], U. Stolzenberg[1], I. Ambrozova[4], M. Sommer[4], J. Slegl[4], J. Solc[5], A. Gkikoudi[6], A. G. Georgakilas[6], A. Papayannis[7,8], and F. S. Krasniqi[1]

[1]Physikalisch-Technische Bundesanstalt (PTB), Braunschweig, Germany, [2]Solar-Terrestrial Center of Excellence and Space Physics, Royal Belgian Institute for Space Aeronomy (BIRA-IASB), Brussels, Belgium, [3]Earth and Life Institute—Climate Sciences (ELI-C), Université Catholique de Louvain, Louvain-la-Neuve, Belgium, [4]The Nuclear Physics Institute of the Czech Academy of Sciences UJF CAS, Prague, Czechia, [5]Czech Metrology Institute, Brno, Czech Republic, [6]DNA Damage Laboratory, Physics Department, School of Applied Mathematical and Physical Sciences, National Technical University of Athens (NTUA), Zografou, Greece, [7]Laser Remote Sensing Unit, Department of Physics, National & Technical University of Athens, Zografou, Greece, [8]Laboratory of Atmospheric Processes and Their Impacts, School of Architecture, Civil and Environmental Engineering, École Polytechnique Fédérale de Lausanne, Lausanne, Switzerland

Key Points:

- Monte Carlo model using Monte Carlo N-Particle and radiosonde/NRLMSISE data was developed to predict altitude-dependent muon flux and energy spectra
- The model captures key atmospheric effects on secondary cosmic rays, including barometric coefficient and seasonal muon flux variations
- The model can link with dosimetry models to assess biological effects of SCR, including DNA damage and long-term health risks

Correspondence to:
A. Al-Qaaod and F. S. Krasniqi,
amer.al-qaaod@ptb.de;
faton.krasniqi@ptb.de

Citation:
Al-Qaaod, A., Pierrard, V., Winant, A., Stolzenberg, U., Ambrozova, I., Sommer, M., et al. (2025). Correlation patterns of muon flux with vertical atmospheric profiles: Insights from Monte Carlo simulations. *Journal of Geophysical Research: Space Physics*, *130*, e2025JA034303. https://doi.org/10.1029/2025JA034303

Received 10 JUN 2025
Accepted 17 OCT 2025

Author Contributions:
Conceptualization: A. Al-Qaaod, V. Pierrard, A. Winant, U. Stolzenberg, I. Ambrozova, M. Sommer, J. Slegl, J. Solc, A. Gkikoudi, A. G. Georgakilas, A. Papayannis, F. S. Krasniqi
Data curation: A. Al-Qaaod, V. Pierrard, A. Winant, U. Stolzenberg, I. Ambrozova, M. Sommer, J. Slegl, A. Gkikoudi, A. Papayannis, F. S. Krasniqi
Formal analysis: A. Al-Qaaod, V. Pierrard, A. Winant, U. Stolzenberg, I. Ambrozova, M. Sommer, J. Slegl, A. G. Georgakilas, A. Papayannis, F. S. Krasniqi
Investigation: A. Al-Qaaod, V. Pierrard, A. Winant, U. Stolzenberg, J. Solc, F. S. Krasniqi

© 2025. The Author(s).
This is an open access article under the terms of the Creative Commons Attribution License, which permits use, distribution and reproduction in any medium, provided the original work is properly cited.

Abstract

The production, attenuation, and absorption of secondary cosmic rays (SCR) are influenced by atmospheric parameters such as air pressure and temperature. To reliably correlate SCR flux measurements with atmospheric ionization driven by energetic particle precipitation, these dependencies must be quantified. Monte Carlo simulations enable detailed modeling of stochastic interactions between cosmic radiation and atmospheric components, providing a robust framework for analyzing underlying physical processes and predicting SCR flux under varying atmospheric conditions. This study introduces a simulation model based on the Monte Carlo N-Particle (MCNP) code, integrating atmospheric profiles from radiosonde data to model the production, absorption, and attenuation of SCR. The model's accuracy was validated through comparisons with the PHITS (Particle and Heavy Ion Transport code System)-based Analytical Radiation Model in the Atmosphere (PARMA) and experimental ground-based muon count measurements. It was subsequently used to investigate the dependence of muon flux on atmospheric pressure and temperature up to 20 km altitude. Results reveal a complex relationship between muon flux and atmospheric variables, particularly in the troposphere and lower stratosphere, where pressure correlations and barometric coefficients exhibit both positive and negative values depending on altitude. The model provides a valuable tool for investigating interactions between SCR and climate variables such as humidity and cloud coverage. Furthermore, the model can be coupled with dosimetry models to assess the biological effects of SCR, including deoxyribonucleic acid (DNA) damage, genomic instability, cellular dysfunction, and long-term health risks such as cancer.

Plain Language Summary

High-energy space particles known as cosmic rays strike Earth's atmosphere and produce secondary particles such as muons. Temperature and air pressure in particular affect how many of these particles make it to the ground. Using actual weather data from weather balloons, we employed a computer simulation (MCNP) to model the motion of cosmic rays through the atmosphere. In order to test our model, we compared it to both real ground-based muon measurements and other simulation models. The findings demonstrate that the correlation between atmospheric conditions and muon levels varies with altitude and is more intricate than anticipated. While increased atmospheric pressure at the ground level leads to reduced muon flux, this correlation shifts with altitude and changes sign above the tropopause. With the use of this model, we can better understand how cosmic rays interact with the atmosphere and investigate how they affect human health and climate particularly radiation exposure during air travel.

1. Introduction

Secondary cosmic rays arise from the interactions of primary cosmic rays (PCR)—predominantly high-energy protons from solar and extraterrestrial sources—with the Earth's atmosphere. These interactions trigger extensive particle cascades, producing protons, neutrons, electrons, muons, and other subatomic particles (Gaisser et al., 2016; Grieder, 2001; Mironova et al., 2015). Among these, muons are particularly prominent due to their high abundance and penetrating ability. Capable of reaching the Earth's surface and even subsurface depths,

Methodology: A. Al-Qaaod, V. Pierrard, A. Winant, U. Stolzenberg, F. S. Krasniqi
Resources: A. Al-Qaaod, V. Pierrard, A. Winant, U. Stolzenberg, I. Ambrozova, M. Sommer, J. Slegl, J. Solc, A. Gkikoudi, A. G. Georgakilas, F. S. Krasniqi
Software: A. Al-Qaaod, V. Pierrard, A. Winant, J. Solc, F. S. Krasniqi
Supervision: F. S. Krasniqi
Validation: A. Al-Qaaod, V. Pierrard, A. Winant, U. Stolzenberg, F. S. Krasniqi
Visualization: A. Al-Qaaod, F. S. Krasniqi
Writing – original draft: A. Al-Qaaod, V. Pierrard, I. Ambrozova, J. Solc, A. G. Georgakilas, A. Papayannis, F. S. Krasniqi
Writing – review & editing: U. Stolzenberg, M. Sommer, J. Slegl, A. Gkikoudi

muons constitute the most readily detectable component of SCR. They are useful across diverse scientific and technological domains, from probing fundamental physics, such as testing quantum chromodynamics models (Albrecht et al., 2022), to practical applications such as muon radiography of volcanic structures and muon tomography for nuclear waste monitoring and characterization (Giammanco, 2022; Mahon et al., 2019; Thompson et al., 2021).

The high penetrating power of muons, which is due to their small stopping power and the effects of relativistic time dilation (Grieder, 2001; Groom et al., 2001), makes them ideal natural probes for detecting dynamic atmospheric changes over time. Although muons have a rest-frame lifetime of only about 2.2 μs, their velocities near the speed of light extend their observed lifetime in Earth's frame. For example, a 4 GeV muons generated at altitudes of around 15 km can still reach the Earth's surface, as their decay time is dilated by a Lorentz factor $\gamma \approx 39$, allowing them to live long enough—up to ∼85 μs in the lab frame—to travel the distance. Continuous monitoring of muon flux at various altitudes could provide real-time insights into the thermal structure of the stratosphere, potentially serving as an indicator of events such as sudden stratospheric warming (Tramontini et al., 2019).

The integration of muon data into atmospheric and climate science could open new pathways for understanding the interplay between cosmic radiation, atmospheric chemistry, and climate variability. Muons, as a proxy for cosmic ray activity, can help quantify the ionization rate in different layers of the atmosphere. The observed fluxes can be integrated into atmospheric models to estimate the production of free radicals, their relation to cosmic events (e.g., solar particle events and geomagnetic storms) and their impact on ozone chemistry. This approach is being currently explored in the European Partnership on Metrology (EPM) joint research project BIOSPHERE, which aims to develop the necessary instrumentation, methods, and measurement infrastructure to assess how the increasing ionization of the atmosphere, caused by extraterrestrial radiation fields (cosmic rays and solar ultraviolet radiation) and amplified by anthropogenic emissions, affects the human and ecological health of our planet [EURAMET 21GRD02 BIOSPHERE] (https://euramet-biosphere.eu/index.php/publis). This collaborative effort among European metrological institutes and scientific organizations focuses on characterizing the relationships between SCR, PCR, Total Ozone Column (TOC), Ultraviolet (UV) radiation, and atmospheric parameters through field measurements. These measurements are facilitated by sophisticated instrumentation, including novel mobile SCR muon and neutron detectors, cutting-edge semiconductor detectors, and light detection and ranging systems tailored for vertical atmospheric profiling (Gidarakou et al., 2024; Kamtchou et al., 2022; Krasniqi et al., 2022; Pierrard et al., 2025).

As muons propagate through the atmosphere, their interactions are influenced by the density distribution of the air (e.g., Winant et al., 2023). As a result, ground-based muon flux measurements capture fluctuations in key atmospheric parameters that affect air density, primarily pressure and temperature, whereas humidity and aerosol concentration contribute only marginally (Maghrabi et al., 2023). It is well established that air pressure plays a crucial role in observed muon flux rates (Wissmann et al., 2005). This is because as air pressure increases, the column of air above the detector becomes denser, acting like a shield that reduces the number of muons that can reach the detector. Dealing with the temperature effect on muons is challenging because it depends on how air is spread out at different heights. Higher temperature at high altitudes makes the air expand, causing fewer hadronic interactions of the particles like π- and K-mesons, which are the major sources of the muons, but also makes muons more likely to decay before they are detected (Tramontini et al., 2019; Wissmann et al., 2005). The overall effect of temperature on muons depends on both how temperature changes with altitude and the energy of the muons. Monte Carlo (MC) simulations, which utilize cross-section data and physics-based models of high-energy particle interactions, combined with vertical atmospheric parameters measured by LIDARs or meteorological radiosondes, enable the separation of atmospheric contributions from genuine cosmic-ray signals. This approach is essential for leveraging muons as a reliable tool for studying atmospheric ionization.

This paper presents an MCNP model for cosmic ray propagation through the atmosphere, incorporating vertical profiles of pressure and temperature measured by meteorological radiosondes. The model predicts the production and transport of various secondary particles, including muons (both positive and negative), neutrons, protons, electrons, positrons, pions (positive and negative, and neutral), kaons (positive, negative, and neutral), and photons, which play a crucial role in assessing cosmic-ray-induced atmospheric ionization and its impact on atmospheric dynamics. The model was used to decode the pressure effects from the measured muon flux rate during the BIOSPHERE measurement campaign in Brussels (Pierrard et al., 2025). Using the measured pressure

21699402, 2025, 11, Downloaded from https://agupubs.onlinelibrary.wiley.com/doi/10.1029/2025JA034303, Wiley Online Library on [29/10/2025]. See the Terms and Conditions (https://onlinelibrary.wiley.com/terms-and-conditions) on Wiley Online Library for rules of use; OA articles are governed by the applicable Creative Commons License

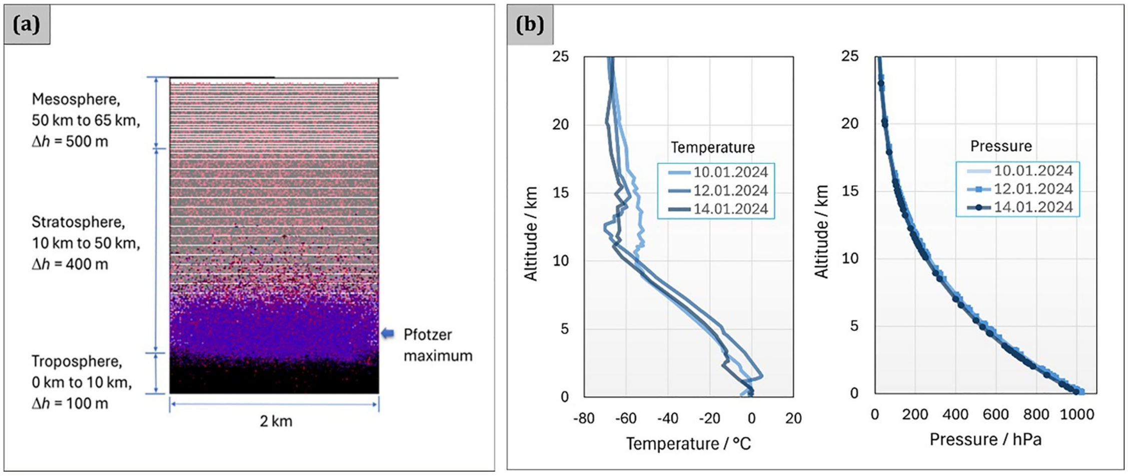

Figure 1. (a) Monte Carlo N-particle visualization with the particle display mode showing the schematics of geometry of the atmosphere and distribution of particles. The Pfotzer maximum marks the altitude where the production of secondary particles reaches its peak. (b) Examples of temperature and pressure distribution versus altitude over Brussels taken from the meteorological sounding database (https://weather.uwyo.edu/upperair/sounding.html).

and atmospheric profiles over Brussels, the atmospheric effects on the measured muon count rate could be simulated. Additionally, the model was used to simulate time-dependent muon count rates at different altitudes, which were then utilized to determine the barometric coefficient as a function of height. Furthermore, by employing constant pressure and temperature profiles, the dependence of the barometric coefficient on cut-off rigidity was investigated. This study focuses on validating the model using experimental muon data from a 3-month BIOSPHERE measurement campaign in Brussels, together with well-established physical principles. Future work will extend the study to atmospheric ionization and correlations between primary and secondary cosmic ray fluxes. In the present analysis, the barometric effect was chosen as a robust benchmark: the pressure effect on muon flux is immediate and directly proportional to the additional atmospheric overburden, expressed in g cm^{-2} (e.g., a pressure swing of ∼20 hPa ≈ 20.4 g cm^{-2} over a week leads to a clearly observable ∼4% change in flux). To illustrate the model's sensitivity to temperature, we include simulations comparing summer and winter flux profiles, which demonstrate that the approach captures the seasonal variations associated with the stratospheric temperature. Importantly, temperature profiles are fully incorporated into the simulations, as they are required both for muon production and for correct treatment of the barometric effect. However, short-term variations (day-to-day or over a 3-month period) are insufficient to determine a reliable temperature coefficient, since stratospheric temperature effects evolve only on seasonal or synoptic timescales and require at least a full year of data and dedicated correction procedures.

This paper is organized as follows: Section 2 describes the details of the simulation geometry and cosmic source definitions. Section 3 discusses the results, including comparisons with measured muon rates, PARMA simulations (Sato, 2015), and a correlation analysis of muon flux with atmospheric pressure. The barometric coefficient is determined from simulations across different altitudes, with ground-level values benchmarked against experimental data. Additionally, its dependence on varying cutoff rigidities is explored to assess the effects of primary proton spectrum truncation, and the relevance of SCR simulation for biological systems is discussed. Finally, Section 4 concludes the study and gives an outlook on potential future developments.

2. Simulation

2.1. Atmosphere Model

The simulation of atmospheric propagation of incoming cosmic rays and their resulting air showers was carried out using the general-purpose ionization radiation transport code Monte-Carlo N-Particle (MCNP) version 6.1, a tool validated for cosmic ray applications (Garrett & Gregg, 2014; Goorley et al., 2013; Gregg, 2013). The atmosphere was modeled as a rectangular prism extending from sea level to an altitude of 65 km, with a base area of 2 km × 2 km. This prism was divided horizontally into 230 cells to reflect variations in atmospheric conditions, such as density and air composition (Figure 1a). The lateral boundaries were treated as void surfaces, allowing

21699402, 2025, 11, Downloaded from https://agupubs.onlinelibrary.wiley.com/doi/10.1029/2025JA034303, Wiley Online Library on [29/10/2025]. See the Terms and Conditions (https://onlinelibrary.wiley.com/terms-and-conditions) on Wiley Online Library for rules of use; OA articles are governed by the applicable Creative Commons License

secondary particles to exit the volume without artificial reflection. Reflective boundaries were not applied, as they can lead to artificial particle accumulation and do not represent real atmospheric conditions (Kulesza et al., 2024). The lateral extent of the simulation volume was optimized such that the contribution of laterally entering particles was negligible compared to the dominant vertical flux. This setup ensures that only particles produced within the column or entering above are tracked.

For the simulation of the atmosphere, radiosonde data (vertical temperature and pressure profiles) over Brussels, provided in the open access database maintained by the University of Wyoming's Department of Atmospheric Science Atmospheric Soundings (https://weather.uwyo.edu/upperair/sounding.html), were utilized (Figure 1b shows the temperature and pressure profiles for 3 days in January 2024). The data for the selected 33 days were used to calculate vertical air density using the ideal gas law up to 26 km altitude. Above that height, the density values from the Naval Research Laboratory Mass Spectrometer and Incoherent Scatter Radar (NRLMSISE) model were used, available through NASA's website (https://ccmc.gsfc.nasa.gov/models/NRLMSIS~00/#outputs), tailored to the specific dates and Brussels' geographical coordinates. The atmospheric data over Brussels was specifically selected because during the time period from January 2024 to March 2024, the 2nd BIOSPHERE measurement campaign to identify and quantify the relationship between cosmic rays, UV radiation and the thickness of the ozone shield was taking place at the urban Brussels region, where two institutes involved in the project, the Belgian Institute for Space Aeronomy (BIRA-IASB) and the Royal Meteorological Institute of Belgium (IRM-KMI), are located. This campaign involved the simultaneous use of numerous optical instruments such as radiometers, spectrometers and pyranometers for accurate spectral and wavelength-integrated measurements of solar UV irradiance, providing access to UV biologically effective dose rate (UV index), TOC and aerosol optical depth, as well as mobile detectors for ground-based secondary cosmic ray measurements (muons and neutrons) (Pierrard et al., 2025). In addition, the campaign was complemented by balloon soundings for vertical profiles of atmospheric parameters, ozone concentration and neutron monitoring provided by the IRM-KMI, and satellite data on energetic particle fluxes measured by GOES and PROBA-V/EPT provided by BIRA-IASB.

In the MCNP input file, density profiles for the model's segments were estimated by interpolating values from both the radiosonde measurements and the NRLMSISE model to ensure matching with the altitudes of the layers in the atmospheric model. At this stage, the atmosphere's composition in the material card was assumed to be uniform across all altitudes, consisting of 75.53% nitrogen, 23.18% oxygen, 1.28% argon, and 0.01% carbon dioxide by weight (carbon dioxide is converted into its elemental composition, carbon, and oxygen, in the material card). The simulation of the atmospheric propagation of high-energy cosmic rays and their cascades utilized MCNP's data libraries and physics models, covering particle energies ranging from approximately 0.1 GeV/n to 1,000 GeV/n. For neutron- and proton-induced reactions, the extended version of Japanese Evaluated Nuclear Data Library Version 4.0 (up to 200 MeV) was chosen, known as JENDL-4.0/HE. For modeling interactions at intermediate and high energies, we employed the intra-nuclear cascade (INC Cascade-Exciton Model (CEM)) and the Los Alamos version of the Quark-Gluon String Model (LAQGSM), respectively.

2.2. Cosmic Source Definition

The most recent MCNP definition of cosmic ray source available in the code includes automatic source normalization, solar modulation, and geomagnetic rigidity cutoff (R_c) of galactic cosmic ray (GCR) spectra (McKinney et al., 2012). The solar modulation potential is integrated into the cosmic ray source and is set to a specific date with the DAT keyword using the parameterized data. The source generates the energy spectrum of protons and alpha particles at 65 km altitude, based on the date and Earth's location. Since protons and alpha particles constitute 99% of primary cosmic rays, it is reasonable to assume that only these particles contribute to the generation of secondary cosmic rays. Figure 2 shows the proton spectra for the selected date of 1 January 2024, which is close to the maximum solar activity of the current solar cycle (designated as Solar Cycle 25), at five different locations in the northern hemisphere, including the cities of Oslo ($R_c \approx 1.4$ GV), Braunschweig ($R_c \approx 2.9$ GV), Brussels ($R_c \approx 3$ GV), Athens ($R_c \approx 8$ GV), and Riyadh ($R_c \approx 14$ GV). The figure shows the progressive clipping of the low-energy galactic spectrum as one moves from low R_c (Oslo), where the magnetic field lines are more perpendicular to the Earth's surface, to high R_c (Riyadh), where the field lines are more parallel to the surface, impeding the entry of cosmic rays into the Earth atmosphere compared to the poles.

21699402, 2025, 11, Downloaded from https://agupubs.onlinelibrary.wiley.com/doi/10.1029/2025JA034303, Wiley Online Library on [29/10/2025]. See the Terms and Conditions (https://onlinelibrary.wiley.com/terms-and-conditions) on Wiley Online Library for rules of use; OA articles are governed by the applicable Creative Commons License

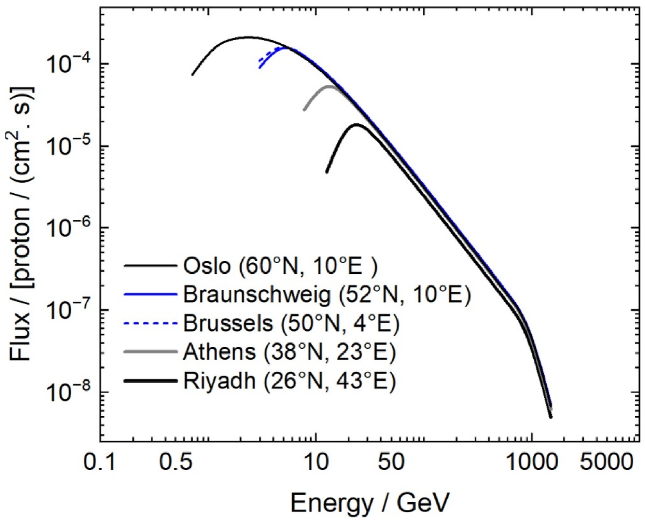

Figure 2. Proton spectra on 1 January 2024, at different latitudes showing the effect of cutoff-rigidity on the primary spectrum.

3. Results and Discussions

3.1. Validation of MCNP Simulations

In this study, 33 input files were run, each corresponding to the vertical pressure and temperature profile of a selected day within the 2nd BIOSPHERE campaign (January 2024 to March 2024). These particular 33 days were chosen due to the notable structures in the observed muon flux. In all input files, 18 particle types were set in the model card and simulated for transport. These include: neutrons, photons, protons, deuterons, tritons, electrons, positrons, muons (μ^- and μ^+), pions (π^+, π^-, and π^0), kaons (K^+ and K^-), anti-protons, anti-neutrons, helium-3 nuclei (^{3}He), alpha particles (^{4}He), and heavy ions. The fluxes of neutrons, muons, protons, electrons, alpha particles, pions, and kaons were scored at 24 different altitudes using the flux-over-a-surface tally. The number of source-particle histories for each of the calculations was 10^9, which resulted in a relative statistical uncertainty of <0.05%. The 33 input files correspond to one file per day, each representing the daily atmospheric profile. The atmospheric pressure and temperature data were obtained from radiosonde measurements at Beauvechain Air Base, Belgium (WMO station 06458, ICAO EBBE). These observations are recorded once daily at 00:00 UTC, providing vertical profiles from the surface to the upper atmosphere. Therefore, the temporal resolution of our atmospheric input data is daily, and the spatial resolution corresponds to the vertical resolution of the radiosonde measurements.

This work will focus solely on the validation of the model using muons, taking the barometric effect as a case study. The barometric effect significantly influences the muon flux observed on the ground and is crucial for disentangling cosmic effects from atmospheric artifacts. The current MCNP model was validated using experimental muon data obtained with the PTB's mobile muon detector DECOS2 (DEtector for COSmic radiation 2) during 33 days from 5 January to 15 February 2024. DECOS2 is a new version of the Physikalisch-Technische Bundesanstalt (PTB) reference detector DECOS1 (Krasniqi et al., 2022), consists of two scintillator-based detection units, each with a 2-dimensional spatially sensitive readout. Each unit contains two crossed layers, each composed of 10 EJ-200 plastic scintillator bars (50 cm long, 5 cm wide and 1 cm thick). This arrangement of scintillator bars, in combination with quadruple coincidence detection (one for each scintillator layer), enables position-sensitive detection with a pixel size of 5 cm × 5 cm. The units can be rotated in space and their separation can be adjusted. The variable distance between the two detector units allows for an adjustable field-of-view (FOV) of the detector. Figure 3 compares the muon flux measured on the Brussels urban site with one simulated using the MCNP model and vertical atmospheric profiling parameters over Brussels (radiosonde data). Simulations compare well with the measured data, with a the reduced c-square (c-square per degree of freedom) $\chi^2_\nu = \sum_i \left[(O_i - E_i)^2 / (\nu \cdot \sigma_i^2) \right] \approx 0.33$, with O_i being the measured muon flux, E_i the simulated muon flux, σ_i the uncertainty of the measured data and ν the degree of freedom ($\nu = 33$). For the MCNP6 simulation points in Figure 3, the error bars represent the statistical uncertainties reported by MCNP6 for each tally. MCNP6 provides the relative statistical error R for each result, which we converted to an absolute error via: ($\sigma_{\text{total}} = \text{Flux} \times R$). Positive ($\mu^+$) and negative ($\mu^-$) muons were simulated separately, and their uncertainties were propagated to obtain the total muon flux uncertainty.

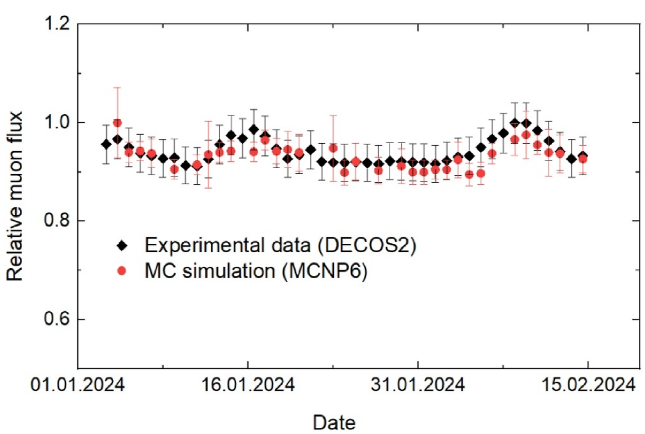

Figure 3. Comparison of the muon flux measured during the 2nd BIOSPHERE measurement campaign in Brussels with the muon flux calculated with the Monte Carlo N-particle model, both fluxes normalized to the maximum value. The simulation model was fed with vertical atmospheric profiles over Brussels, which were measured during the campaign with meteorological radiosonde (see Section 2.1).

Muon spectra simulated using MCNP model were also compared with those from the PHITS-based Analytical Radiation Model in the Atmosphere (PARMA), which was validated using multiple sets of experimental data at nearly the same location and altitude (Sato, 2015, 2016).

21699402, 2025, 11, Downloaded from https://agupubs.onlinelibrary.wiley.com/doi/10.1029/2025JA034303, Wiley Online Library on [29/10/2025]. See the Terms and Conditions (https://onlinelibrary.wiley.com/terms-and-conditions) on Wiley Online Library for rules of use; OA articles are governed by the applicable Creative Commons License

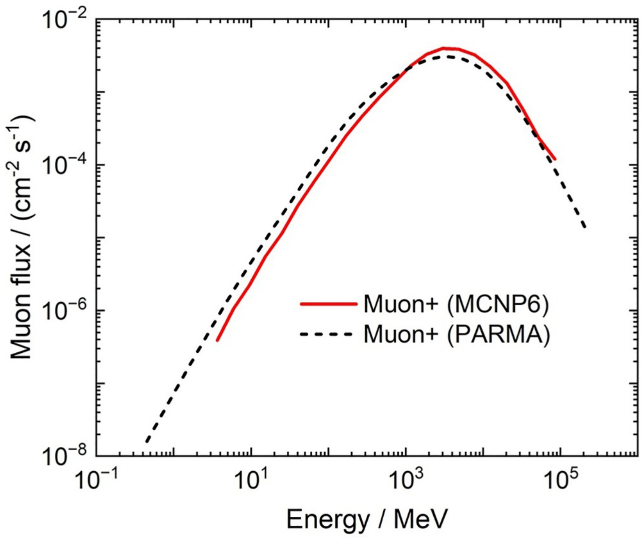

Figure 4. Comparison of the positive muon spectra calculated with Monte Carlo N-Particle (this study) and PARMA (Sato, 2015) at an altitude of 0.2 km and a cutoff rigidity of 8 GV. In both cases, the muon spectrum at this altitude peaks at about 4 GeV.

Figure 4 shows the comparison of muon plus (μ^+) spectra simulated using the MCNP model and PARMA as implemented in EXcel-based Program for calculating Atmospheric Cosmic-ray Spectrum (EXPACS) for the selected altitude of 0.2 km and location (cutoff rigidity) at ~8 GV. One can observe the good agreement between the two, although minor discrepancies between MCNP and PARMA are likely due to the different models employed. In MCNP, the CEM physics model is used for intermediate energy interactions, and LAQGSM for high energy scenarios. Additionally, atmospheric densities and temperatures in MCNP are derived from actual radiosonde measurements up to an altitude of about 26 km. Above this altitude, density values from the NRLMSISE model are used. Conversely, in the PARMA model, densities and temperatures are based on the US Standard Atmosphere 1976. Furthermore, while PARMA considers GCR protons and heavy ions with charges up to 28 (Ni) as source particles, MCNP only accounts for proton and alpha spectra.

3.2. Relative Variation of Muon Flux and Energy Spectra With Altitude

In the simulation, the muon flux was scored at 24 height levels from the ground surface up to a height of 25 km. The initial altitudes were set to 0, 0.1, 0.2, 0.5, 1, 3, 5, 7 and 10 km, while for the remining altitudes the step size was varied between 0.8 and 1 km. All muon flux values presented in this work are normalized to their respective maximum values to highlight relative variations with altitude, season, and atmospheric conditions. In Figure 5, the values are shown for selected days at various altitudes, alongside the corresponding vertical atmospheric temperature profiles. Each curve corresponds to a different day and illustrates the muon flux variation with temperature across altitudes. Starting from an altitude of about 25 km, the results show the peak at about 15 km, which is known as the Pfotzer maximum (Grieder, 2001). Beyond this point, at lower altitudes, absorption and decay of muons start to take over and the muon flux begins to reduce. Both pressure and temperature profiles are essential inputs to the simulation to predict the muon flux at the ground level. Pressure determines the total atmospheric overburden that muons must traverse, while temperature modifies the altitude–density profile of the atmosphere and thereby shifts the effective production height of muons. The upward shift of the muon production layer, Δh, can be approximated as $\Delta h \approx h_0\ \Delta T/T_0$, where h_0 is the mean production altitude at temperature T_0 (Wissmann et al., 2005). For example, if $h_0 = 12$ km and $\Delta T/T_0 = 4\%$, the production layer Δh rises by about 500 m. This additional distance is significant: muons with energies around 1.9 GeV, which are already close to their decay threshold, would not survive the extra path length and therefore would not reach the ground.

For temperature effects to become clearly visible in muon data, two conditions must be met: (a) sufficiently large variations in the effective temperature, which is a weighted average stratospheric temperature that indicates how favorable the atmosphere is for pions and kaons to decay into muons instead of reinteracting (typically on the order of 10–15 K), and (b) a consistent temporal trend. During January and February 2024 data sets (see Figure 5a), for instance, the effective temperature variations are typically below 6 K, with only occasional increases up to ~12 K. Such fluctuations are often masked by barometric pressure changes and by statistical uncertainties in the muon counting rate, making it impossible to extract a reliable temperature coefficient during the time the experiment campaign was carried out. Ground-level temperature variations do not play a role since muons are produced much higher in the atmosphere. It is the stratospheric temperature that matters, and this evolves only on seasonal or synoptic time scales. That's exactly what is observed in muon seasonal modulation studies (Wissmann et al., 2005); Arunbabu et al., 2017)].

In the present work, the influence of temperature expressed through the temperature coefficient has not been isolated from pressure effects, as such a determination requires at least one full year of observations and dedicated correction procedures. This would constitute a substantial follow-up study beyond the scope of the current work. To illustrate the model's sensitivity to temperature and the importance of including realistic temperature profiles in the simulations, we have performed simulations for both summer and winter conditions. The corresponding

21699402, 2025, 11, Downloaded from https://agupubs.onlinelibrary.wiley.com/doi/10.1029/2025JA034303, Wiley Online Library on [29/10/2025]. See the Terms and Conditions (https://onlinelibrary.wiley.com/terms-and-conditions) on Wiley Online Library for rules of use; OA articles are governed by the applicable Creative Commons License

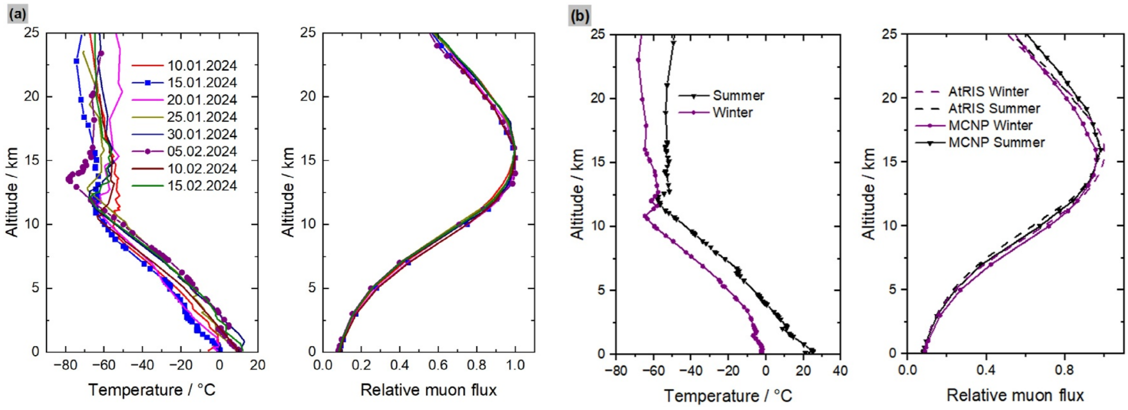

Figure 5. (a) Variation of the measured atmospheric temperature and simulated muon flux with altitude. The temperature profiles represent measurements with radiosondes during selected days in winter. (b) Seasonal (summer and winter) variations in atmospheric temperature and the corresponding normalized muon flux with altitude. The results of AtRIS for the summer and winter profiles of 2024 are also illustrated for comparison.

results (see Figure 5b) demonstrate that the model captures the seasonal changes associated with the effective temperature. To make these subtle seasonal differences clearer, Figure 6 shows the flux ratio $\Phi_{\text{winter}}/\Phi_{\text{summer}}$ as a function of altitude. The results reveal that the muon flux is slightly higher in winter than in summer at lower altitudes (below ∼12 km). This is explained by the upward shift of the production layer in summer: muons must travel a longer distance to reach the ground, and more of them decay in flight. Consequently, the ground-level muon flux in winter is about 3.6% higher than that in summer, in good agreement with the measurements reported by Wissmann et al. (2005).

Figure 5b also presents muon flux profiles simulated using AtRIS (Atmospheric Radiation Interaction Simulator; Banjac, Herbst, & Heber, 2019,Banjac, Herbst, Heber, Berger, & Burmeister, 2019; Winant et al., 2023) with protons and alpha particles as primary inputs. The same atmospheric profile used in the MCNP simulations was applied in AtRIS; however, the atmosphere was extended to 100 km altitude and discretized into 200 layers, each 500 m thick. The recommended GEANT-4 physics list for AtRIS was used (Winant & Pierrard, 2025). Primary particle energies ranged from 1 MeV to 1 TeV, distributed across 120 energy bins. To compute the muon flux, the GCR spectrum was derived using the Force Field Approximation, based on the local interstellar spectrum from Herbst et al. (2017), with a modulation potential of $\varphi = 820$ MV corresponding to 1 January 2024. The resulting muon profiles qualitatively agree with those obtained from the MCNP model for both summer and winter conditions, with minor quantitative differences (up to 7%) attributable to differing assumptions between the two simulation approaches.

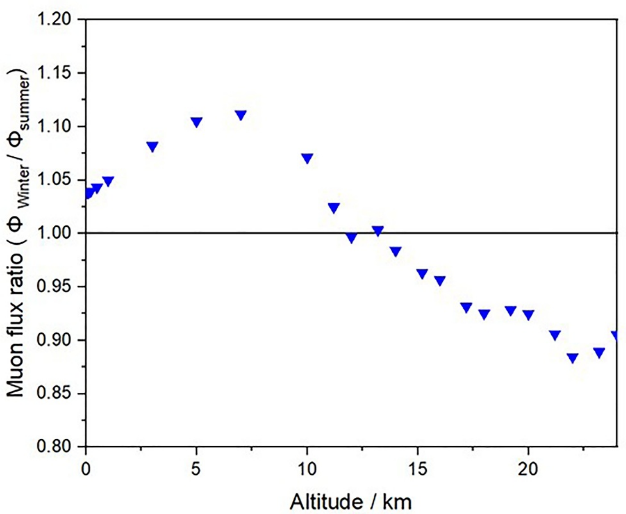

Figure 6. Ratio of simulated muon flux in winter to summer ($\Phi_{\text{winter}}/\Phi_{\text{summer}}$) as a function of altitude. A value greater than one indicates higher muon flux in winter, while values below one indicate higher flux in summer.

The effects of absorption and decay are best illustrated in the muon spectra presented in Figure 7. Energy spectra for both positive and negative muons were scored at various altitudes for the atmospheric profiles over Brussels corresponding to 15 January 2024. The figure demonstrates a progressive shift in the peak of the muon distribution, from approximately 0.7 GeV at the Pfotzer maximum to around 4 GeV at an altitude of 100 m. This shift is accompanied by a significant decrease in muon flux, which drops by more than an order of magnitude from 15.2 to 0.1 km. While muons lose energy as they traverse the atmosphere, the flux at lower altitudes is dominated by higher-energy muons, which are less likely to decay due to time dilation effects, allowing them to penetrate deeper into the atmosphere. In contrast, lower-energy muons are more likely to decay before reaching these altitudes, contributing to the observed upward shift at higher altitudes. The charge asymmetry in cosmic ray-induced muons arises because cosmic rays, which are mostly high-energy protons, collide with atmospheric nuclei and preferentially produce more positively charged mesons, pion plus (π^+) and kaon plus (K^+), than their negative counterparts.

21699402, 2025, 11, Downloaded from https://agupubs.onlinelibrary.wiley.com/doi/10.1029/2025JA034303, Wiley Online Library on [29/10/2025]. See the Terms and Conditions (https://onlinelibrary.wiley.com/terms-and-conditions) on Wiley Online Library for rules of use; OA articles are governed by the applicable Creative Commons License

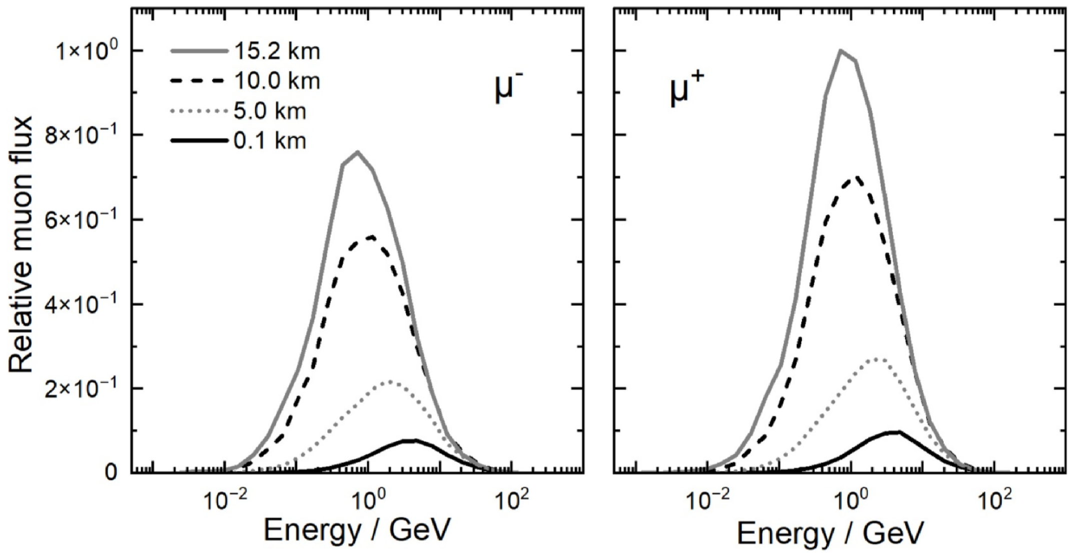

Figure 7. Simulated energy spectra of negative and positive muons scored at four different altitudes.

3.3. Correlation Analysis

The SCR flux measured on the ground is intrinsically linked to the flux and energy spectrum of primary cosmic radiation (Gaisser et al., 2016). While PCR initiates the production of SCR through nuclear interactions in the atmosphere, the resulting SCR flux is modulated by atmospheric parameters such as pressure and temperature, solar activity, and geomagnetic effects (Grieder, 2001). Although the correlation of SCR flux with these effects is established to a considerable degree, refining the empirical models relating SCR flux observed on the ground with atmospheric parameters would enable incorporating real-time atmospheric data to improve the accuracy of SCR predictions and also to use SCR fluxes as a data channel for climate science.

Variation in the atmospheric pressure and temperature can cause considerable changes in the muon flux measured on the ground. To compare measurements taken at different times or locations, these pressure-induced variations must be accounted for. This will allow separation of atmospheric effects from the genuine cosmic ray variations such as Forbush decrease or ground level enhancements. Figure 8 presents the raw muon and neutron count rates measured during the BIOSPHERE campaign in Brussels using PTB's muon detector DECOS2 and the neutron monitor in Dourbes, which is part of the Real-time Neutron Monitor Database (NMDB) (Mavromichalaki et al., 2011) https://www.nmdb.eu/nest/. In both cases, a clear anticorrelation with atmospheric pressure is observed. A pressure decrease of approximately 40 hPa results in an increase of more than 8% in the muon count rate and over 27% in the neutron count rate. Pressure changes dominate the effect of atmosphere in the measured muon flux due to their influence on atmospheric density and cosmic ray interaction probabilities.

Temperature, while less significant, introduces additional variability, especially in the stratosphere. The temperature dependence of SCR flux is more complex than that of pressure. An increase in temperature typically lowers the air density. When this happens in the stratosphere, it leads to the upward expansion of the air and the rise of the muon production layer. Temperature changes in the troposphere, on the other hand, are more related to the absorption of muons through air density changes and are often intrinsically encoded in the pressure effects (e.g., during air mass movements). Here we explore only correlation effects related to pressure.

Figure 9 shows the muon flux scored at different altitudes, from 0.1 to 16 km. Each simulation data point represents the relative flux rate over Brussels, with atmospheric profiles (pressure and temperature) from radiosonde measurements taken over the same location. The maximum flux value at 16 km was used as the reference for normalizing the muon flux values at all altitudes in Figure 9. This common normalization standard ensures direct comparability across different altitudes. The absolute value of the reference flux used for normalization was 0.12836 $cm^{-2}\ s^{-1}$. Figure 10 shows the same data, plotted as muon flux versus atmospheric pressure, together with their linear fits obtained using ordinary least squares regression and the corresponding relative uncertainties. From both Figures, it is evident that below 10.5 km, atmospheric pressure is well anticorrelated with the muon

21699402, 2025, 11, Downloaded from https://agupubs.onlinelibrary.wiley.com/doi/10.1029/2025JA034303, Wiley Online Library on [29/10/2025]. See the Terms and Conditions (https://onlinelibrary.wiley.com/terms-and-conditions) on Wiley Online Library for rules of use; OA articles are governed by the applicable Creative Commons License

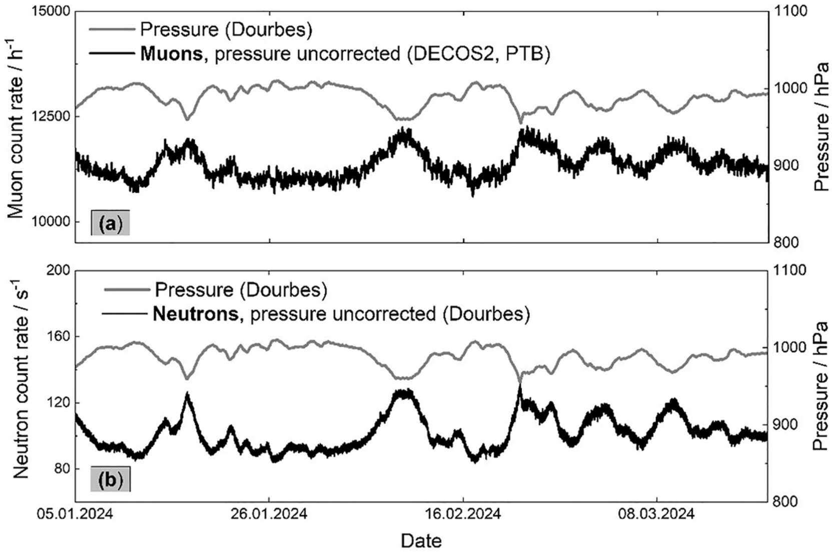

Figure 8. Anticorrelation of the secondary cosmic rays flux with atmospheric pressure. (a) Muons measured with DECOS2 during the Brussels measurement campaign and (b) neutrons measured with the neutron monitor in Dourbes, which is part of the real-time neutron monitor database.

flux, as expected and measured (see Figure 8). At higher altitudes, however, a positive correlation appears between atmospheric pressure and muon flux. This relationship is illustrated in Figure 11, which displays the Pearson correlation coefficient for muon flux and atmospheric pressure up to an altitude of 20 km.

This effect is also reflected in the barometric coefficient, which is needed to correct the pressure effects in the observed muon data. Figure 11 also shows the barometric coefficient as a function of altitude over Brussels. At the ground level, the barometric coefficient is determined to be $\beta_P = (-0.14 \pm 0.02)\%\ hPa^{-1}$, consistent with the empirical value $-0.145\%\ hPa^{-1}$ predicted by the empirical curve in Mendonça et al. (2019) for a cutoff rigidity of $R_c = 3.2$ GV (specific to Brussels). The values deduced with SEVAN detectors (Chilingarian & Karapetyan, 2011) at altitudes of 1,000 m, 2,000 m, and 3,200 m are $(-0.149 \pm 0.035)\%\ hPa^{-1}$, $(-0.242 \pm 0.022)\%\ hPa^{-1}$, and $(-0.351 \pm 0.038)\%\ hPa^{-1}$, respectively, and are shown in Figure 11. The values at 1,000 m and 2,000 m compare well with our simulation results of $-0.17\%\ hPa^{-1}$ and $-0.21\%\ hPa^{-1}$, respectively, while at 3,200 m the calculated value of $-0.25\%\ hPa^{-1}$ shows a somewhat larger relative difference (≈28%). Nevertheless, all experimentally deduced barometric coefficients confirm the same decreasing trend with altitude.

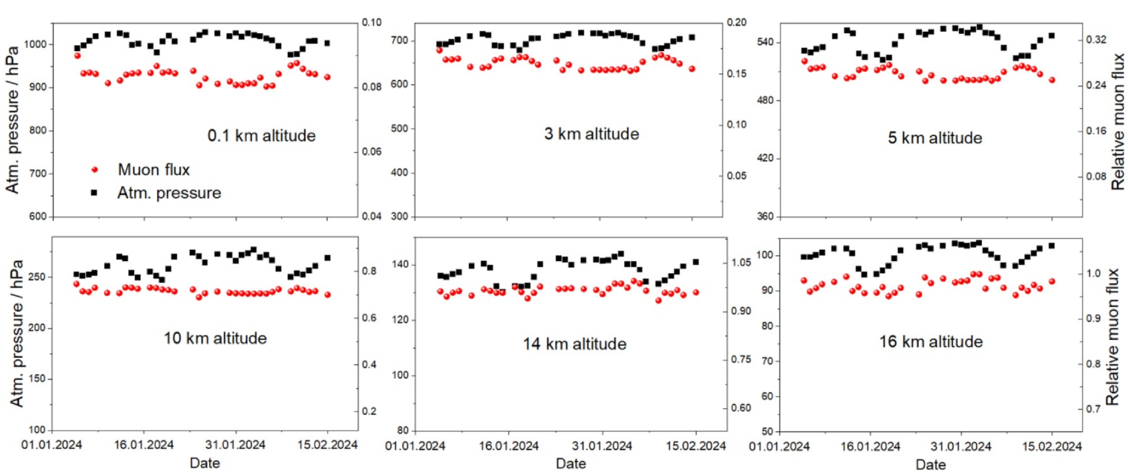

Figure 9. Comparison of simulated muon with atmospheric pressure at different altitudes. Below 10.5 km, the muon flux and pressure exhibit an inverse correlation, whereas above this altitude, they show a positive correlation, meaning that the muon flux rate and pressure follow the same temporal trend.

21699402, 2025, 11, Downloaded from https://agupubs.onlinelibrary.wiley.com/doi/10.1029/2025JA034303, Wiley Online Library on [29/10/2025]. See the Terms and Conditions (https://onlinelibrary.wiley.com/terms-and-conditions) on Wiley Online Library for rules of use; OA articles are governed by the applicable Creative Commons License

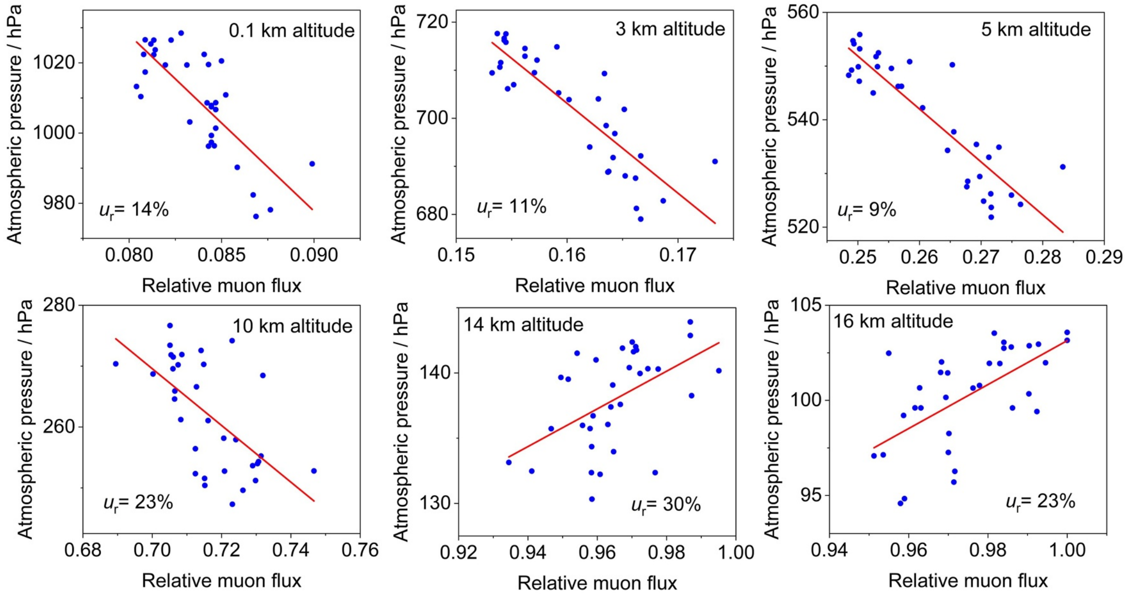

Figure 10. Scatter plots of the relative muon fluxes (I/I_{ref}, with $I_{ref} = 0.12836\ cm^{-2}\ s^{-1}$) shown in Figure 8 as a function of atmospheric pressure. The red lines represent linear fits obtained using ordinary least squares regression. The relative uncertainties u_r of the fitted slopes are reported in each panel. At low altitudes (0.1–10 km), the slopes are negative, indicating the expected inverse correlation between muon flux and pressure. However, above ∼10.5 km (14 and 16 km panels), the slopes become positive reflecting a reversal in the pressure dependence.

Although these data were obtained at higher cutoff rigidity, we show below that cutoff rigidity has no significant influence on the barometric coefficient.

The dependence on the altitude reflects the dependence of muon flux with altitude (see Figure 5a). The change in the sign of the barometric coefficient near 10.5 km coincides with the altitude of the tropopause in the atmospheric

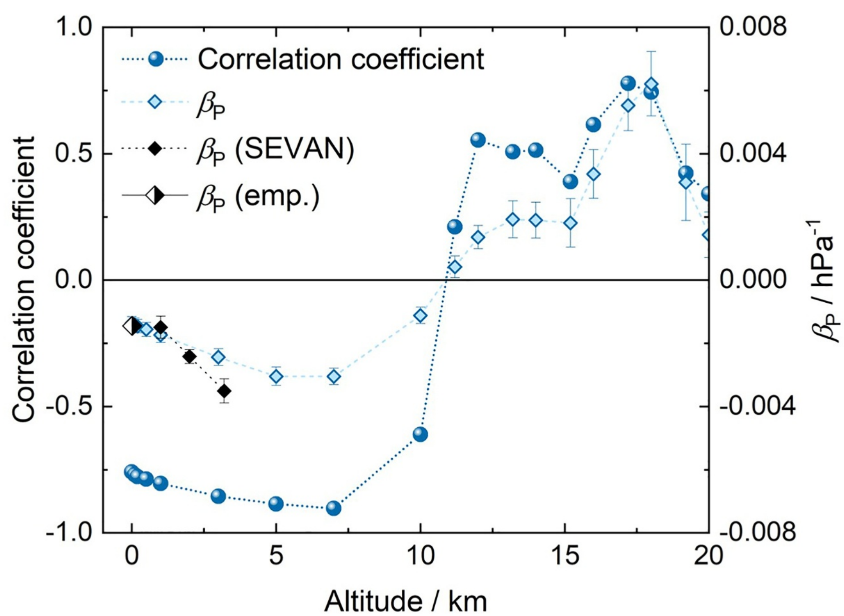

Figure 11. Pearson correlation coefficient between atmospheric pressure and muon flux rate, and barometric coefficient ($\beta_P = \left(\Delta\dot{\phi}/\dot{\phi}\right)/\Delta p$, with $\dot{\phi}$ being the muon flux rate and Δp being the change in atmospheric pressure) as a function of altitude. The values of the barometric coefficient deduced from measurements with SEVAN detectors are shown as black diamonds, while the value predicted by the empirical model of Mendonça et al. (2019) is shown as a half-filled diamond.

21699402, 2025, 11, Downloaded from https://agupubs.onlinelibrary.wiley.com/doi/10.1029/2025JA034303, Wiley Online Library on [29/10/2025]. See the Terms and Conditions (https://onlinelibrary.wiley.com/terms-and-conditions) on Wiley Online Library for rules of use; OA articles are governed by the applicable Creative Commons License

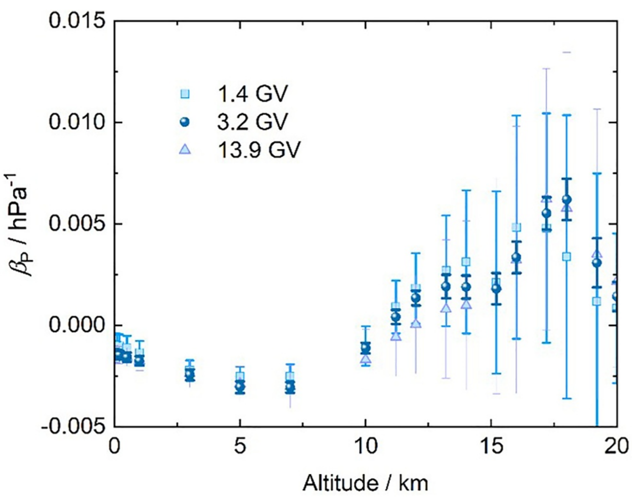

Figure 12. Barometric coefficient, β_P, utilizing atmospheric profiles over Brussels but with variations in the truncation of the primary cosmic ray spectrum achieved by adjusting the cutoff rigidity.

profiles used. Since most muons are produced above this altitude, no significant new contribution to the muon budget occurs below it; instead, muons only undergo increasing energy loss and decay as the overlying atmospheric mass grows with decreasing altitude. Consequently, muon flux decreases as pressure increases, resulting in a negative correlation. Above 10.5 km, and particularly above the Pfotzer maximum, muon production is substantial because as the atmosphere becomes denser with the decreasing altitude, more primary protons interact with it and produce pions, and thus more pions decaying into muons. In this region, muon flux increases with decreasing altitude, same as pressure increases with decreasing altitude, leading to a positive correlation. The vertical temperature and pressure profiles derived from radiosonde data directly determine both the altitude of the tropopause and the atmospheric density gradient, thereby controlling the precise altitude of this sign reversal.

Figure 12 presents the barometric coefficient as a function of altitude for different cutoff rigidities, which account for the truncation of the primary cosmic ray spectrum due to Earth's magnetic field. Each simulation point is derived using the same vertical atmospheric profiles as in Figure 11. The objective is to demonstrate the altitude dependence of the barometric coefficient by exclusively varying the cutoff rigidity (i.e., truncating the primary cosmic ray spectrum) without introducing additional atmospheric parameters as degrees of freedom. The barometric coefficient generally exhibits a slight increase with higher cutoff rigidity (R_c) (Mendonça et al., 2019). However, for altitudes below the tropopause, the changes in the barometric coefficient fall within the uncertainties caused by fluctuations in atmospheric parameters. This behavior could be well related to the fact that all simulations employ the same vertical profiles of pressure and temperature.

3.4. Relevance of SCR Simulation for Biological Systems

SCRs, including muons, neutrons, and protons, are believed to have significant—primarily detrimental—effects on living organisms, including humans and animals (Atri & Melott, 2014). Exposure to these particles increases the risk of cancer and other health issues due to their ionizing nature and the complex molecular damage they can inflict on DNA, RNA, proteins, and lipids. Although cosmic muons on the ground have relatively low LET compared to neutrons and protons, their high energy and ability to produce secondary particles (e.g., electrons) enhance their radiobiological potential, contributing to DNA damage (de Groen, 2022). Research suggests that the pattern of DNA mutations linked to human diseases corresponds with the expected effects of continuous muon flux, indicating a possible connection between muon-induced DNA damage and processes such as aging, evolution, and disease incidence—particularly during periods of elevated cosmic ray exposure, such as solar events (Pierrard et al., 2025). Furthermore, when muon flux is combined with high-energy protons and other ionizing components—as often occurs during solar particle events—the overall biological impact is amplified, as demonstrated in the recent paper by Gkikoudi et al. (2025).

Therefore, simulating SCR is essential for understanding and predicting their biological impact, particularly during solar particle events when radiation intensities can surge by several orders of magnitude. Because direct measurements during solar events are limited and often unavailable in critical locations (e.g., upper atmosphere, space habitats, or even high-altitude regions), simulations provide a vital tool for estimating radiation dose, particle penetration, and secondary particle production in realistic biological scenarios.

4. Conclusions

A MC simulation model for secondary cosmic ray (SCR) propagation through the atmosphere was developed using the MCNP code version 6.1. The model integrates atmospheric pressure and temperature profiles from radiosonde data up to 26 km altitude, with the NRLMSISE model applied for higher altitudes. It accurately predicts muon flux in regions where atmospheric profiling parameters are valid. The muon flux energy spectra produced by the model align well with those from the PHITS-based Analytical Radiation Model in the Atmosphere (PARMA). This study explored muon flux, energy spectra, and their correlation with vertical atmospheric

21699402, 2025, 11, Downloaded from https://agupubs.onlinelibrary.wiley.com/doi/10.1029/2025JA034303, Wiley Online Library on [29/10/2025]. See the Terms and Conditions (https://onlinelibrary.wiley.com/terms-and-conditions) on Wiley Online Library for rules of use; OA articles are governed by the applicable Creative Commons License

21699402, 2025, 11, Downloaded from https://agupubs.onlinelibrary.wiley.com/doi/10.1029/2025JA034303, Wiley Online Library on [29/10/2025]. See the Terms and Conditions (https://onlinelibrary.wiley.com/terms-and-conditions) on Wiley Online Library for rules of use; OA articles are governed by the applicable Creative Commons License

temperatures at various altitudes. The ground level barometric coefficient determined from simulations at a cutoff rigidity of $R_c = 3.2$ GV, $\beta_P = (-0.0014 \pm 0.0002)$ hPa^{-1}, is consistent with the value reported in the literature (Mendonça et al., 2019). The model also correctly predicts the seasonal variations in the muon flux. For example, about 3.6% more muons are observed on the ground in winter than in summer, which also agrees well with previous experimental observations (Wissman, 2006). The simulations reveal a negative correlation between muon flux and atmospheric pressure below the tropopause (around 10.5 km) and a positive correlation above it. These findings validate the model's ability to capture key phenomena and the complex interplay between temperature and muon flux across different atmospheric layers. By employing accurate source definition and atmospheric profiling parameters, the model effectively distinguishes genuine cosmic ray effects from atmospheric influences. Furthermore, SCR simulations using this approach can be used to support risk assessment and mitigation strategies in aviation, space exploration, and high-altitude living. They also offer a framework for understanding the long-term biological consequences of repeated or chronic low-dose exposure, contributing to research in aging, evolution, and disease mechanisms.

Conflict of Interest

The authors declare no conflicts of interest relevant to this study.

Data Availability Statement

The atmospheric sounding data used in the simulations are publicly available from the University of Wyoming (2024). Neutron monitor data from Dourbes were obtained from the Neutron Monitor Database (NMDB) (2024). Processed muon flux results, experimental muon count rates collected during the BIOSPHERE campaign, and supporting data sets are openly available in Zenodo (Al-Qaaod, 2025b). The corresponding MC simulation input model (MCNP6) is also available in Zenodo (Al-Qaaod, 2025a). Atmospheric model data were obtained from NASA's Community Coordinated Modeling Center (CCMC) NRLMSISE-00 model (Picone et al., 2002).

Acknowledgments
The project (21GRD02 BIOSPHERE) has received funding from the European Partnership on Metrology, co-financed by the European Union's Horizon Europe Research and Innovation Programme and by the Participating States. Funded by the European Union. Views and opinions expressed are, however, those of the author(s) only and do not necessarily reflect those of the European Union or EURAMET. Neither the European Union nor the Granting authority can be held responsible for them. A. Al-Q. and F. S. K. thank the staff of the High-Performance Computing (HPC) group in PTB Berlin for their support with the use of the computing cluster. Open Access funding enabled and organized by Projekt DEAL.

References

Albrecht, J., Cazon, L., Dembinski, H., Fedynitch, A., Kampert, K. H., Pierog, T., et al. (2022). The muon puzzle in cosmic-ray induced air showers and its connection to the large hadron collider. *Astrophysics and Space Science*, *367*(3), 27. https://doi.org/10.1007/s10509-022-04054-5

Al-Qaaod, A. (2025a). MCNP6 simulation input model for altitude-dependent muon flux in the atmosphere [Software]. *Zenodo*. https://doi.org/10.5281/zenodo.17301024

Al-Qaaod, A. (2025b). Processed muon flux results and experimental muon count rates from the BIOSPHERE campaign [Dataset]. *Zenodo*. https://doi.org/10.5281/zenodo.15630977

Arunbabu, K. P., Ahmad, S., Chandra, A., Dugad, S. R., Gupta, S. K., Hariharan, B., et al. (2017). Dependence of the muon intensity on the atmospheric temperature measured by the GRAPES-3 experiment. *Astroparticle Physics*, *94*, 22–28. https://doi.org/10.1016/j.astropartphys.2017.07.002

Atri, D., & Melott, A. L. (2014). Cosmic rays and terrestrial life: A brief review. *Astroparticle Physics*, *53*(C), 186–190. https://doi.org/10.1016/J.ASTROPARTPHYS.2013.03.001

Banjac, S., Herbst, K., & Heber, B. (2019). The atmospheric radiation interaction simulator (AtRIS): Description and validation. *Journal of Geophysical Research: Space Physics*, *124*(1), 50–67. https://doi.org/10.1029/2018ja026042

Banjac, S., Herbst, K., Heber, B., Berger, L., & Burmeister, S. (2019). On-the-fly calculation of absorbed and equivalentatmospheric radiation dose in a water phantomwith the atmospheric radiation interactionsimulator (AtRIS). *Journal of Geophysical Research: Space Physics*, *124*(12), 50–67. https://doi.org/10.1029/2019ja026622

Chilingarian, A., & Karapetyan, T. (2011). Calculation of the barometric coefficients at the start of the 24th solar activity cycle for particle detectors of aragats space environmental center. *Advances in Space Research*, *47*(7), 1140–1146. https://doi.org/10.1016/j.asr.2010.12.001

de Groen, P. C. (2022). Muons, mutations, and planetary shielding. *Frontiers in Astronomy and Space Sciences*, *9*, 1067491. https://doi.org/10.3389/fspas.2022.1067491

Gaisser, T. K., Engel, R., & Resconi, E. (2016). *Cosmic rays and particle physics*. Cambridge University Press. https://doi.org/10.1017/CBO9781139192194

Garrett, E., & Gregg, W. (2014). *MCNP6 cosmic and terrestrial background particle fluxes - Release 4' (no. LA-UR-14-24445)*. Los Alamos National Laboratory (LANL).

Giammanco, A. (2022). Muon Imaging: Present Status and Emerging Applications.

Gidarakou, M., Papayannis, A., Kokkalis, P., Evangeliou, N., Vratolis, S., Remoundaki, E., et al. (2024). Optical and microphysical properties of the aerosols during a rare event of biomass-burning mixed with polluted dust. *Atmosphere*, *15*(2), 190. https://doi.org/10.3390/atmos15020190

Gkikoudi, A., Manda, G., Beinke, C., Giesen, U., Al-Qaaod, A., Dragnea, E. M., et al. (2025). Synergistic effects of UVB and ionizing radiation on human non-malignant cells: Implications for ozone depletion and secondary cosmic radiation exposure. *Biomolecules*, *15*(4), 536. https://doi.org/10.3390/biom15040536

Goorley, J. T., James, M. R., Booth, T. E., Brown, F. B., Bull, J. S., Cox, L. J., et al. (2013). Initial MCNP6 release overview-MCNP6 version 1.0 (no. LA-UR-13-22934). NM (United States).

Gregg, W. (2013). MCNP simulations of background particle fluxes from galactic cosmic rays. In *Transactions of the American nuclear society annual meeting* (Vol. 108, pp. 651–654).
Grieder, P. K. F. (2001). *Cosmic rays at Earth*. Elsevier.
Groom, D. E., Mokhov, N. V., & Striganov, S. I. (2001). Muon stopping power and range tables 10 MeV–100 TeV. *Atomic Data and Nuclear Data Tables*, *78*(2), 183–356. https://doi.org/10.1006/ADND.2001.0861
Herbst, K., Muscheler, R., & Heber, B. (2017). The new local interstellar spectra and their influence on the production rates of the cosmogenic radionuclides ^{10}Be and ^{14}C. *Journal of Geophysical Research: Space Physics*, *122*(1), 23–34. https://doi.org/10.1002/2016ja023207
Kamtchou, B., Jakubek, J., Soukup, P., Jakubek, M., Turecek, D., Marek, L., et al. (2022). Spectral tracking of energetic charged particles in wide field-of-view with miniaturized telescope MiniPIX Timepix 3 1×2 stack. *Journal of Instrumentation*, *17*(3), C03028. https://doi.org/10.1088/1748-0221/17/03/C03028
Krasniqi, F., Stolzenberg, U., Luchkov, M., Morosh, V., Kramer, P., Kahnt, K., et al. (2022). PTB metrological infrastructure for the environmental dose assessment. Retrieved from https://inis.iaea.org/records/pymbr-brs52
Kulesza, J. A., Adams, T. R., Armstrong, J. C., Bolding, S. R., Brown, F. B., Bull2024). *MCNP® Code Version 6.3.1 Theory and User Manual* (Vol. 1). Los Alamos National Laboratory Technical Report, LA-UR-24-24602, Rev.
Maghrabi, A. H., Alzahrani, S. A., & Alruhaili, A. S. (2023). The role of atmospheric pressure, temperature, and humidity on cosmic ray muons at a low latitude station. *International Journal of Astronomy and Astrophysics*, *13*(3), 236–258. https://doi.org/10.4236/IJAA.2023.133014
Mahon, D., Clarkson, A., Gardner, S., Ireland, D., Jebali, R., Kaiser, R., et al. (2019). First-of-a-kind muography for nuclear waste characterization. *Philosophical Transactions of the Royal Society A*, *377*(2137), 20180048. https://doi.org/10.1098/RSTA.2018.0048
Mavromichalaki, H., Papaioannou, A., Plainaki, C., Sarlanis, C., Souvatzoglou, G., Gerontidou, M., et al. (2011). Applications and usage of the real-time neutron monitor database. *Advances in Space Research*, *47*(12), 2210–2222. https://doi.org/10.1016/J.ASR.2010.02.019
McKinney, G., Armstrong, H., James, M., Clem, J., & Goldhagen, P. (2012). *MCNP6 cosmic-source option' (no. LA-UR-12-22318)*. Los Alamos National Laboratory (LANL).
Mendonça, R. R. S., Wang, C., Braga, C. R., Echer, E., Dal Lago, A., Costa, J. E. R., et al. (2019). Analysis of cosmic rays' atmospheric effects and their relationships to cutoff rigidity and zenith angle using global muon detector network data. *Journal of Geophysical Research: Space Physics*, *124*(12), 9791–9813. https://doi.org/10.1029/2019JA026651
Mironova, I. A., Aplin, K. L., Arnold, F., Bazilevskaya, G. A., Harrison, R. G., Krivolutsky, A. A., et al. (2015). Energetic particle influence on the earth's atmosphere. *Space Science Reviews*, *194*(1–4), 1–96. https://doi.org/10.1007/s11214-015-0185-4
Neutron Monitor Database (NMDB). (2024). Dourbes neutron monitor data [Dataset]. *Neutron Monitor Database (NMDB)*. Retrieved from https://www.nmdb.eu
Picone, J. M., Hedin, A. E., Drob, D. P., & Aikin, A. C. (2002). NRLMSISE-00 empirical model of the atmosphere: Statistical comparisons and scientific issues [Software]. *NASA Community Coordinated Modeling Center*, *107*(A12), SIA15-1–SIA15-16. https://doi.org/10.1029/2002ja009430
Pierrard, V., Bolsée, D., Winant, A., Al-Qaaod, A., Krasniqi, F., de Bonhome, M. P., et al. (2025). BIOSPHERE measurement campaign from January 2024 to March 2024 and in May 2024: Effects of the solar events on the radiation belts, UV radiation and ozone in the atmosphere. *AIMS Geosciences*, *11*(1), 117–154. https://doi.org/10.3934/GEOSCI.2025007
Sato, T. (2015). Analytical model for estimating terrestrial cosmic ray fluxes nearly anytime and anywhere in the world: Extension of PARMA/EXPACS. *PLoS One*, *10*(12), 1–33. https://doi.org/10.1371/journal.pone.0144679
Sato, T. (2016). Analytical model for estimating the zenith angle dependence of terrestrial cosmic ray fluxes. *PLoS One*, *11*(8), 1–22. https://doi.org/10.1371/journal.pone.0160390
Thompson, L., Aymanns, K., Niemeyer, I., Vieh, C., & Weekes, M. (2021). The use of muon radiography in safeguarding geological repositories. *Safety of Nuclear Waste Disposal*, *1*, 279–280. https://doi.org/10.5194/sand-1-279-2021
Tramontini, M., Rosas-Carbajal, M., Nussbaum, C., Gibert, D., & Marteau, J. (2019). Middle-atmosphere dynamics observed with a portable muon detector. *Earth and Space Science*, *6*(10), 1865–1876. https://doi.org/10.1029/2019EA000655
University of Wyoming. (2024). Upper air sounding data archive [Dataset]. *University of Wyoming*. Retrieved from https://weather.uwyo.edu/upperair/sounding.html
Winant, A., Pierrard, V., Botek, E., & Herbst, K. (2023). The atmospheric influence on cosmic-ray-induced ionization and absorbed dose rates. *Universe*, *9*(12), 502. https://doi.org/10.3390/universe9120502
Winant, M., & Pierrard, V. (2025). Good practice guide for the simulation and estimation of particle fluxes during minimum solar activity, maximum solar activity and the recent solar energetic particle events. *Zenodo*. https://doi.org/10.5281/zenodo.16992405
Wissmann, F. (2006). Variations observed in environmental radiation at ground level. *Radiation Protection Dosimetry*, *118*(1), 3–10. https://doi.org/10.1093/rpd/nci317
Wissmann, F., Dangendorf, V., & Schrewe, U. (2005). Radiation exposure at ground level by secondary cosmic radiation. *Radiation Measurements*, *39*(1), 95–104. https://doi.org/10.1016/J.RADMEAS.2004.03.025

21699402, 2025, 11, Downloaded from https://agupubs.onlinelibrary.wiley.com/doi/10.1029/2025JA034303, Wiley Online Library on [29/10/2025]. See the Terms and Conditions (https://onlinelibrary.wiley.com/terms-and-conditions) on Wiley Online Library for rules of use; OA articles are governed by the applicable Creative Commons License